



Fenton-like catalysis by MnO_2 membrane reactor with oxygen vacancies for carbamazepine degradation



Yichuan Wang ^{a,1}, Tianlin Zhou ^{a,1}, Dezhi Chen ^{a,*}, Zhi-Xia Zhang ^a, Quanzhi Zhang ^a, Xinchun Ye ^a, Jianjun Wan ^b, Jian-Ping Zou ^{a,*}

^a Key Laboratory of Jiangxi Province for Persistent Pollutants Prevention Control and Resource Reuse, School of Environmental and Chemical Engineering, Nanchang Hangkong University, Nanchang 330063, China

^b State Key Laboratory of Nuclear Resources and Environment, East China University of Technology, Nanchang 330013, China

ARTICLE INFO

ABSTRACT

Keywords:
Peroxymonosulfate activation
Heterogeneous catalyst
Manganese dioxide
Non radical pathway
Oxygen vacancies

Pathway design for singlet oxygen (${}^1\text{O}_2$) with in-situ regulation has shown great interest for peroxy monosulfate (PMS) activation toward advanced oxidation in water treatment. Herein, we propose a facile method to design MnO_2 catalysts with tunable surface oxygen vacancies (OVs) concentration to achieve radical-to-nonradical pathway transition. The surface of the OVs-rich NFM-140 provides an optimal site for PMS adsorption and allows $\bullet\text{OH}$ to break through the energy demand limitation and preferentially convert to ${}^1\text{O}_2$ for electrophilic attack to pollutants. This OVs-regulated oxidation system can selectively switch to the ${}^1\text{O}_2$ -dominated nonradical pathway in response to pollutant recalcitrance, perfectly eliminating the pollutants and transforming them into the harmless products. Our research presents a novel perspective on the selective generation of reactive oxygen species (ROS) for the degradation of organic pollutants in PMS by utilizing the mediation of OVs.

1. Introduction

The application of peroxyomonosulfate (PMS) in advanced oxidation processes holds significant promise for water treatment due to its impressive capacity to eliminate and mineralize pollutants [1,2]. Heterogeneous transition metal-based catalysts have a stable structure and high efficiency, which contributes to their exceptional catalytic activity towards PMS [3–5]. Manganese oxide, especially MnO_2 , are widely used as catalyst due to its exceptional stability, activity, and cost-efficiency among transition metal oxides [4,6]. The interplay of radical and non-radical processes empowers the PMS-based heterogeneous oxidation system to effectively target and degrade trace pollutants present in complex water matrices [7,8]. However, the presence of co-existing ions and organics can interfere with non-selective radicals (SO_4^{2-} and $\bullet\text{OH}$) that impede the elimination of the target pollutants [9]. Concurrently, the PMS/catalyst system offers alternative non-radical pathways, such as singlet oxygen (${}^1\text{O}_2$), electron-mediated transfer [10], and oxidation by high-valent metal species [11], that exhibit extraordinary capability in selectively degrading electron-rich pollutants and resisting interference [12]. Therefore, the search for stable oxidation system with highly

efficient non-radical pathway is still ongoing.

The introduction of defect engineering to introduce oxygen vacancies (OVs) provides a method for regulating the properties of bulk catalysts to achieve non-radical pathways. This approach has demonstrated significant potential in controlling the intrinsic electronic properties of materials, creating active sites, and optimizing the porous structure [13,14]. The introduction of OVs can be achieved through various methods, such as plasma treatment, reduction processes, combinations of metal oxides, ion doping, and thermal treatment [6]. OVs arise from the absence of lattice oxygen on the surface of metal oxides. The creation of OVs allows electrons to approach and occupy the O 2p orbital, causing it to detach from the atomic domain. This alteration causes changes in the physicochemical properties and enhances its electron transfer capabilities and conductivity. OVs elevate the Fermi level of the oxide, leading to the formation of defensive levels within the bandgap and the reduction of the bandwidth, which effectively enhance the activity of catalysts [15,16]. For instance, OVs present in ZFC-20 % can activate ozonation to remove contaminants attributed to the nonradical-based oxygen species of surface atomic oxygen (${}^{\circ}\text{O}$) [17]. The chemical adsorption of O_2 and the generation of ${}^1\text{O}_2$ are enabled by

* Corresponding authors.

E-mail addresses: chendz@nchu.edu.cn (D. Chen), zjp_112@126.com (J.-P. Zou).

¹ These authors contributed equally to this work.

the presence of OVs in α -Bi₂O₃. [18]. $^1\text{O}_2$ is employed as the main reactive species in the OVs-mediated peroxydisulfate (S₂O₈²⁻; PDS) activation process for the degradation of bisphenol A (BPA) under alkaline conditions [19]. This observation highlights the potential strategy of introducing OVs to enhance the catalytic performance of catalyst [19]. OVs on the surface of bulk materials may selectively adsorb and activate to break O-O bonds to produce reactive oxygen species (ROS), but the specific mechanisms involved in the activation of PMS through OVs and the subsequent generation and transformation of ROS remain poorly understood at present.

In this research, we synthesized MnO₂ with tunable oxygen vacancy (OVs) concentrations through a one-step hydrothermal method and assembled it in a membrane reactor to activate PMS for the removal of organic pollutants from aqueous phase. PMS exhibits a strong tendency to adsorb onto the surface of MnO₂ with OVs. As a result, $^1\text{O}_2$ can be rapidly generated through the intermediate mediation of free radicals for the swift removal of carbamazepine (CBZ). We conducted batch experiments to simulate the impact of real water matrices and tested the degradation kinetics of the membrane reactor. Environmental toxicity detection of intermediates was performed to assess its potential application. This study introduces a novel perspective on utilizing OVs to selectively generate ROS for the targeted degradation of organic pollutants.

2. Experimental section

2.1. Chemical materials

In this work, manganese sulfate (MnSO₄, >99.0%), ammonium sulfate ((NH₄)₂SO₄, >99.0%), ammonium persulfate ((NH₄)₂S₂O₈, 99.0%), Oxone peroxymonosulfate (PMS, 42.0–46.0% 2KHSO₅·KHSO₄·KSO₄) were obtained from Alfa Aesar, China. Humic acid (HA, >90.0%), methyl phenyl sulfoxide (PMSO, 99.0%) and methyl phenyl sulfone (PMSO₂, 99.0%), tetracycline (TC, 99.0%), acid orange 7 (AO7, 99.0%), Rhodamine B (RhB, 99.0%), bisphenol A (BPA, 99.0%), 1, 3-diphenylisobenzofuran (DPBF, 97.0%), p-phthalic acid (TA, 99.0%) were acquired from Shanghai Macklin Biochemical Co. Ltd. Methanol (MeOH, 99.0%), tert-butyl-alcohol (TBA, 99.0%), chroloform (99.0%), L-histidine (L-His, 99.0%), carbamazepine (CBZ, 99.0%), and sodium pyrophosphate (PP, 99.0%) were obtained from Sinopharm Chemical Regent Co. Ltd. (Shanghai, China). 2, 2-azino-bis (3-ethylbenzothiazoline)-6-sulfonic acid diammonium (ABTS, 99.0%) was purchased from Sigma-Aldrich. These analytical reagents were used without further purification. Deionized water (18 MΩ cm) was used in the whole experiment process.

2.2. Preparation of nanofiber membrane

First, MnSO₄ (1.208 g), (NH₄)₂S₂O₈ (1.824 g) and (NH₄)₂SO₄ (5.28 g) were dissolved successively in 40 mL of deionized water. The above reaction solution was transferred to a 100 mL Teflon-lined stainless-steel autoclave, which was sealed and placed in an oven at the set temperature for 12 h. After the reaction, the autoclave was allowed to cool naturally to room temperature, and the obtained MnO₂ nanofibers were washed to neutral with deionized water and dried by lyophilization. The nanofiber membrane (NFM) was prepared by vacuum filtration of 50 mg of MnO₂ nanofibers dispersed in deionized water (Scheme S1a). The NFM catalysts using MnO₂ nanofibers obtained at different temperatures (140, 160, 180 and 200 °C) were designated as NFM-140, NFM-160, NFM-180 and NFM-200, respectively.

2.3. Characterizations

The sample morphology and structure were analyzed with an TESCAN MIRA LMS scanning electron microscope (SEM) and an FEI Talos

F200X transmission electron microscope (TEM). The catalyst phase was analyzed on a Bruker D8 Advance X-ray powder diffractometer (XRD). The surface functional groups were studied on a PerkinElmer Fourier-transform infrared spectroscopy (FTIR) accompanied with the range from 4000 to 400 cm⁻¹. The specific surface area and pore size distribution was calculated from N₂ adsorption/desorption isotherm using the Brunauer-Emmett-Teller (BET) and Barrett-Joyner-Halenda theory (BJH) models, respectively. The N₂ adsorption/desorption isotherm was obtained from the Micromeritics TriStar II 3020 surface area and pore size analyzer at 77 K. The surface chemical environment was examined by X-ray photoelectron spectroscopy (XPS) on a Kratos Axis Ultra XPS spectrometer. The interfacial evolution during PMS activation was evaluated by *in situ* Raman spectra on a Raman microscope (Renishaw inVia Raman, Text S1 for details). The leached metal ions were detected with a Bremen Hanna-Kunath-Sir.11, 28199 inductively coupled plasma mass spectrometer (ICP-MS). The concentration of CBZ was detected using high performance liquid chromatography (HPLC, Text S2 for details) and free radicals and non-free radicals generated in degradation were determined using electron paramagnetic resonance (EPR, Text S3 for details). The intermediate products in CBZ degradation were determined using liquid chromatography mass spectrometry (LC-MS, Text S4 for details). Total organic carbon (TOC) in the degradation of CBZ was detected using a Shimadzu TOC-L CPH/CPN analyzer. CHI 760E electrochemical workstation (Shanghai Chenhua, China) was used for all electrochemical measurements (Text S5 for details).

2.4. Evaluation of catalytic performance

The catalytic performance of as-assembled NFM for PMS activation was evaluated using CBZ degradation. CBZ degradation was carried out using a membrane degradation system (Scheme S1b), which included a peristaltic pump, water baths, a membrane reactor and 250 mL beakers. The prepared NFM was positioned inside the membrane reactor. The detailed procedure is as follows. 0.1 g PMS was added to 100 mL CBZ with an initial concentration of 20 mg/L (C₀). The above solution was then pumped through the membrane reactor to initiate the degradation reaction. At certain intervals, 0.5 mL of solution sample was taken and immediately mixed with 0.5 mL of methanol to terminate the reaction. The residual CBZ was determined by HPLC (Text S2). All experiments were performed in triplicate.

2.5. Computational methods

In density function theory (DFT) calculations, structural optimization was performed by Vienna Ab-initio simulation package (VASP) with the projector augmented wave (PAW) method [20]. The exchange-functional was treated using the Perdew-Burke-Ernzerhof (PBE) functional. The DFT-D3 correction was used to describe weak interactions between atoms. Cut-off energy of the plane-wave basis was set as 450 eV and the Brillouin zone integration was performed with a Monkhorst-Pack k-point sampling of 2×3×1. Spin polarization was adopted to describe magnetism of models. Hubbard U correction was introduced to describe strong interactions of Mn-3d orbitals, as U_{Mn} = 3.9 eV [21]. In calculation of Gibbs free energy, the adsorption model was built by employing the computational hydrogen electrode (CHE) model developed by Nørskov, et al [22]. Detailed calculations were described in Text S6.

3. Results and discussion

3.1. Morphology and structure

The NFM membrane catalysts were obtained by vacuum filtration of fibrous α -MnO₂ (Fig. S1), and exhibit a dense reticular structure (Fig. 1a-c) with certain mechanical strength (Fig. S2) and hydrophilicity (Fig. S3) [23]. As shown in Fig. 1d, the typical TEM image reveals that NFM-140

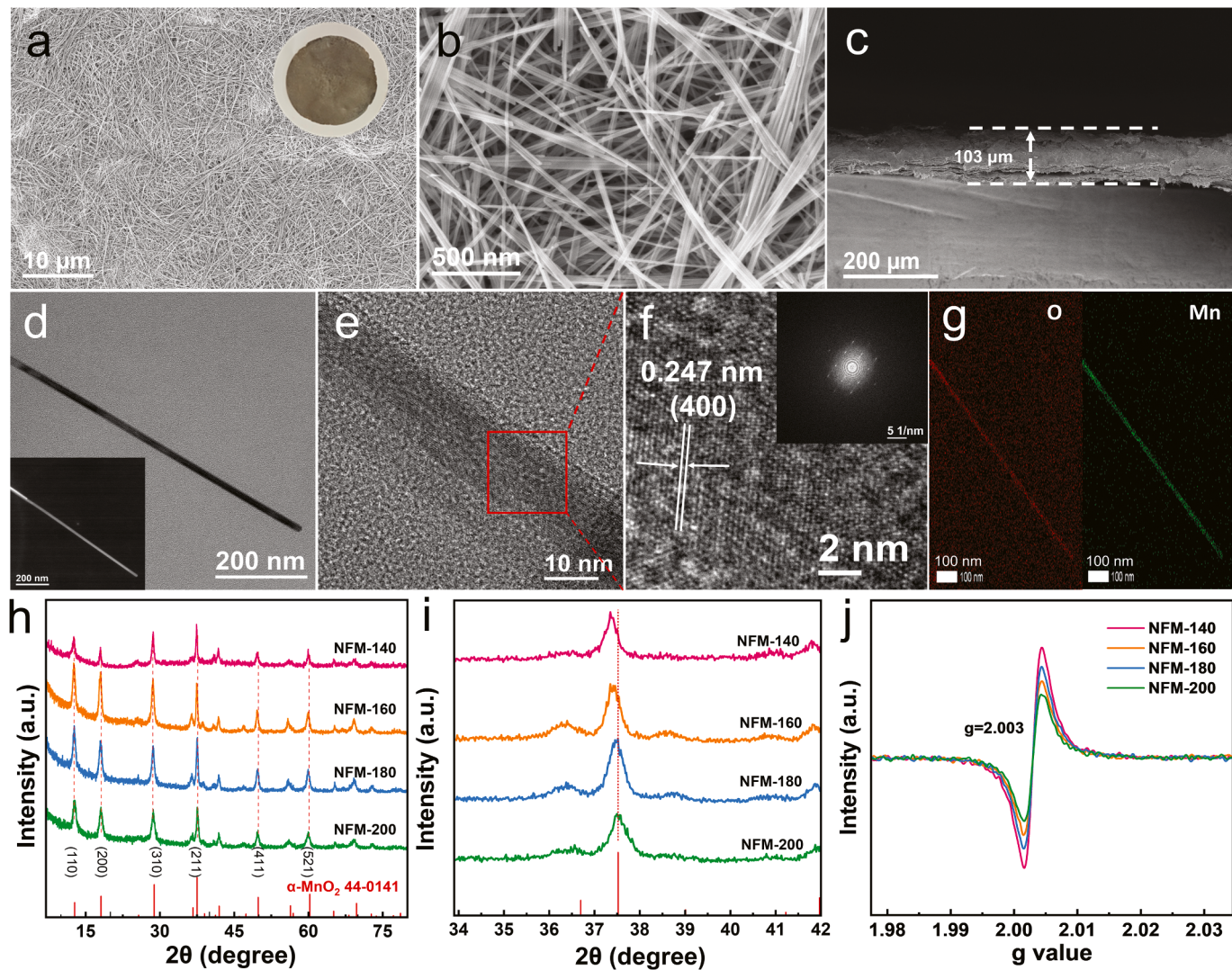


Fig. 1. Characteristics of NFM-140 membranes. a-b, c) SEM images of top view and cross view of the NFM-140 membrane, d) TEM and HADDF inset, e, f) HRTEM and FFT inset, g) HADDF-STEM and EDS mapping images of NFM-140, h) XRD patterns, i) enlarged image of XRD patterns, j) EPR spectra.

features a single crystal structure with a lattice spacing of 0.247 nm (Fig. 1e-f), which is well consistent with the (400) crystal plane of α -MnO₂ (JPCDS No. 44-0141). The Mn and O elements are uniformly distributed in the catalyst from the energy-dispersive X-ray spectroscopy (EDS) mapping (Fig. 1g). The FTIR spectra (Fig. S4) further reveal that the three bands at 464, 514 and 707 cm⁻¹ can be attributed to the stretching mode of Mn-O and deformation mode of Mn-O-Mn in MnO₂ octahedral lattice, respectively [24]. The N₂ adsorption-desorption isotherms with a H3 hysteresis loop and the Type IV characteristic (Fig. S5) show a mesoporous structure of the NFM, and the calculated specific surface area (S_{BET}) and average pore size are presented in Table S1.

XRD patterns were utilized to determine the crystalline phases of the as-prepared catalysts (Fig. 1h). All the diffraction peaks of samples are identical to those of α -MnO₂ (JPCDS No. 44-0141). With the decrease of the reaction temperature, the characteristic diffraction peak of (211) plane gradually shift towards a lower angle (Fig. 1i), indicating a change in the crystal lattice structure possibly attributed to the presence of the OVs [19]. EPR measurements were carried out to analyze the presence of OVs in NFM catalysts (Fig. 1j). The signal at $g=2.003$ indicates the existence of OVs [25]. Furthermore, the decreased reaction temperature is conducive to the generation of OVs, which matches well with the above XRD results.

XPS spectra were acquired to analyze the surface chemical envi-

ronment of the as-prepared catalysts. Fig. S6a displays the survey spectra of as-prepared NFM catalysts. The high-resolution O 1s spectra (Fig. S6b) can be fitted with two obvious peaks at 529.6 and 531.2 eV, corresponding to lattice oxygen (O_L) and adsorbed oxygen species (O_A: O²⁻, O⁻ etc.), respectively [26,27]. The highest O_L/O_A value (Table S2) of NFM-140 suggests more OVs [28]. The result is further confirmed by the valent fitting of Mn 2p spectra (Fig. S6c). The Mn 2p XPS spectra are deconvoluted into three curves concerted at 641.8, 642.9 and 644.5 eV, which can be attributed to the Mn²⁺, Mn³⁺, and Mn⁴⁺ on the surface of the NFM catalysts, respectively [29]. The content of Mn with different valences was calculated by the integral area of curves (Table S2), and NFM-140 possesses the highest Mn³⁺ content of 55.3%. According to previous studies, OVs would be generated to maintain electrostatic balance once Mn³⁺ was presented in MnO₂ [30]. Mn³⁺ would elongate the Mn-O bond due to the Jahn-Teller effect, the longer length of Mn-O bond and the weaker interaction between Mn and O atoms contributed to the formation of OVs [31]. Based on the above discussion, the Mn³⁺ content on the MnO₂ surface can represent the concentration of OVs [32]. The high concentration of Mn³⁺ and O_L/O_A ratios indicate a higher abundance of OVs on the surface of NFM-140, agreeing well with the EPR results.

3.2. Catalytic performance of NFM

The catalytic performance of as-prepared NFM catalysts was examined in the degradation of CBZ by activating PMS. The degradation curves presented in Fig. 2a demonstrate that NFM-140/PMS can remove 96.7% of CBZ in 25 min. Simultaneously, the removal efficiency of CBZ by the adsorption is low to 1.5%, and only 5.0% CBZ is removed through the oxidation by single PMS. The corresponding first-order kinetic constant (k) is shown in Fig. 2b. The highest k value (0.157 min^{-1}) for NFM-140/PMS underlines the dominant role of NFM-140 in the enhancement of the oxidation of CBZ by PMS. In addition, as displayed in Fig. 2c, the catalytic performance of NFM is compared with other MnO_x and membrane catalysts reported in recent literature shown in Table S3. The order of magnitude dominance of k values and removal efficiencies in PMS/pollutants system highlight the viability of the NFM membrane reactors.

The physicochemical properties of NFM catalysts were correlated to the k of the CBZ removal. The desirable S_{BET} of catalyst provides an abundance of undercoordinated surface atoms to bind to reactant molecules [33]. Despite NFM-140 with the best performance possesses a high specific surface area ($79.8 \text{ m}^2/\text{g}$), the lack of correlation between surface area and k indicates that S_{BET} does not contribute to activity differences (Fig. S7a). In comparison, the addition of OVs to the surface of NFM significantly enhances its ability to activate PMS. Electrochemical impedance spectroscopy (EIS) (Fig. S8, Table S4) indicates that the introduction of OVs interfere with the charge-transfer resistance (R_{ct}) of NFM. The fitting results of the equivalent circuit model show that the high concentration of OVs imparts the NFM with a greater electron transport capability (Fig. S7b). The strong correlation between OVs intensity and k ($R^2 = 0.977$) in Fig. S7c indicates that OVs is crucial for the activation of PMS.

3.3. Identification of ROS and pathway

Scavenging experiments and EPR were carried out to identify the predominant ROS responsible for CBZ degradation. Tert-butyl alcohol (TBA) is effective in quenching $\bullet\text{OH}$, and methanol (MeOH) can be used as scavenger to quantify the contribution of $\text{SO}_4^{\bullet-}$ and $\bullet\text{OH}$ [34]. Chloroform and L-His are scavengers of $\text{O}_2^{\bullet-}$ and $^1\text{O}_2$, respectively [35,36]. MeOH demonstrates only a marginal inhibitory effect on degradation, and TBA has negligible impact on the degradation process (Fig. 3a-b, Figs. S9a-b). Free radicals can bind to the catalyst surface, except at high concentrations of hydrophilic TBA [37]. Therefore, KI was used to remove surface-bound free radicals (Fig. S10). The introduction of KI confirms the presence of radicals (including $\bullet\text{OH}$ bound to the material

surface). The narrow seven-line EPR spectrum (1:2:1:2:1:1:2:1) was obtained from the oxidation of excess DMPO by $\bullet\text{OH}$ and $\text{SO}_4^{\bullet-}$ (Fig. 3e) [38]. $\bullet\text{OH}$ could be verified by the specific fluorescence probe (Text S7) [39]. Specifically, the fluorescence signal for 2-hydroxy terephthalic acid detected at 465 nm in the NFM-140/PMS system serves as the evidence for the presence of $\bullet\text{OH}$ (Fig. 3c).

Combined results of radical scavenging and fluorescence detection, we speculate that $\bullet\text{OH}$ is not involved in the degradation process but are more likely as a transition state ROS. Breaking the chemical bonds of organic pollutants makes them more susceptible to further oxidation and decomposition can also be achieved by $\text{O}_2^{\bullet-}$ [40]. The ignorable quenching by chloroform (5–20 mM) and undetectable DMPO– $\text{O}_2^{\bullet-}$ as well as the NBT probe experiment (Fig. 3f, Fig. S9c and Fig. S11) verify the absence of $\text{O}_2^{\bullet-}$ in CBZ elimination. In contrast, the inhibitory effects obtained by introducing L-His (Fig. 3a, Fig. S9d), and the DPBF serving as a probe confirm the significant generation of $^1\text{O}_2$ (Fig. 3d, Fig. S12) [41]. The intensity of the 1:1:1 triple peak in the EPR spectra (Fig. 3g) is inhibited by the concentration of L-His, which supports the above findings. The intensity of the $\text{TEMP}^{-1}\text{O}_2$ in NFM-140/PMS/CBZ system is significantly enhanced compared to NFM-200/PMS/CBZ, while a stronger DMPOX is detectable in NFM-200/PMS/CBZ (Fig. 3e and g). It suggests that $^1\text{O}_2$ is the main ROS and the NFM/PMS system with high OVs is conducive to generating more $^1\text{O}_2$.

The dissolved oxygen (DO) may be the potential precursors for $^1\text{O}_2$. As displayed in Fig. S13, the degradation of CBZ remains unaffected when argon or oxygen gas was introduced, indicating that DO is not involved in the production of $^1\text{O}_2$ in the NFM-140/PMS system. $\text{O}_2^{\bullet-}$ could be the intermediate of $^1\text{O}_2$, while it can be excluded because $\text{O}_2^{\bullet-}$ is not detected in the system. The remarkable attenuation of $\text{TEMP}^{-1}\text{O}_2$ signal value after adding the TBA suggests that $\bullet\text{OH}$ might be the precursor for the generation of $^1\text{O}_2$ (Fig. 3g). In addition, the OVs-induced structural distortion results in the release of lattice oxygen atoms from the catalyst surface to be converted to precursor reactive oxygen ($^{\bullet}\text{O}$) of $^1\text{O}_2$ via OVs (Fig. S14a) [42]. Meanwhile, the content of Mn^{3+} and Mn^{4+} in NFM-140 decreases, while the content of Mn^{2+} increases, demonstrating that Mn sites obtain electrons during the oxidation process (Fig. S14b).

In situ Raman spectroscopy was performed to reveal the interfacial evolution during PMS activation over NFM-140. As shown in Fig. S15, the characteristic peaks of PMS at 889 and 1060 cm^{-1} belong to HSO_5^- , the peak at 979 cm^{-1} is assigned to $\text{SO}_4^{\bullet-}$. A new peak at 836 cm^{-1} of a surface-bonded complex ($\text{MnO}_2-(\text{O})\text{OSO}_3^-$) can be observed after adding PMS [32,43]. The intensity of the $\text{MnO}_2-(\text{O})\text{OSO}_3^-$ peak is unaffected by

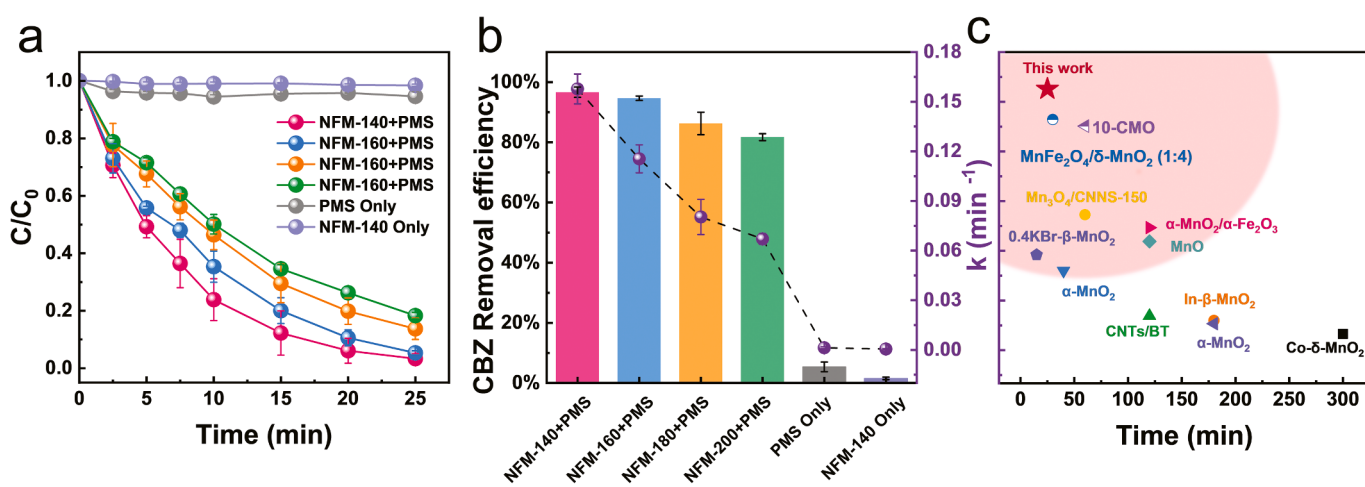


Fig. 2. a) CBZ degradation curve by different NFM/PMS systems. ([Membrane]=0.05 g, [PMS]=1 g/L, [CBZ]=20 mg/L, T=30 °C), b) kinetics rate constant, c) comparison of intrinsic catalytic activity of the NFM membranes with the previously reported catalysts for PMS activation.

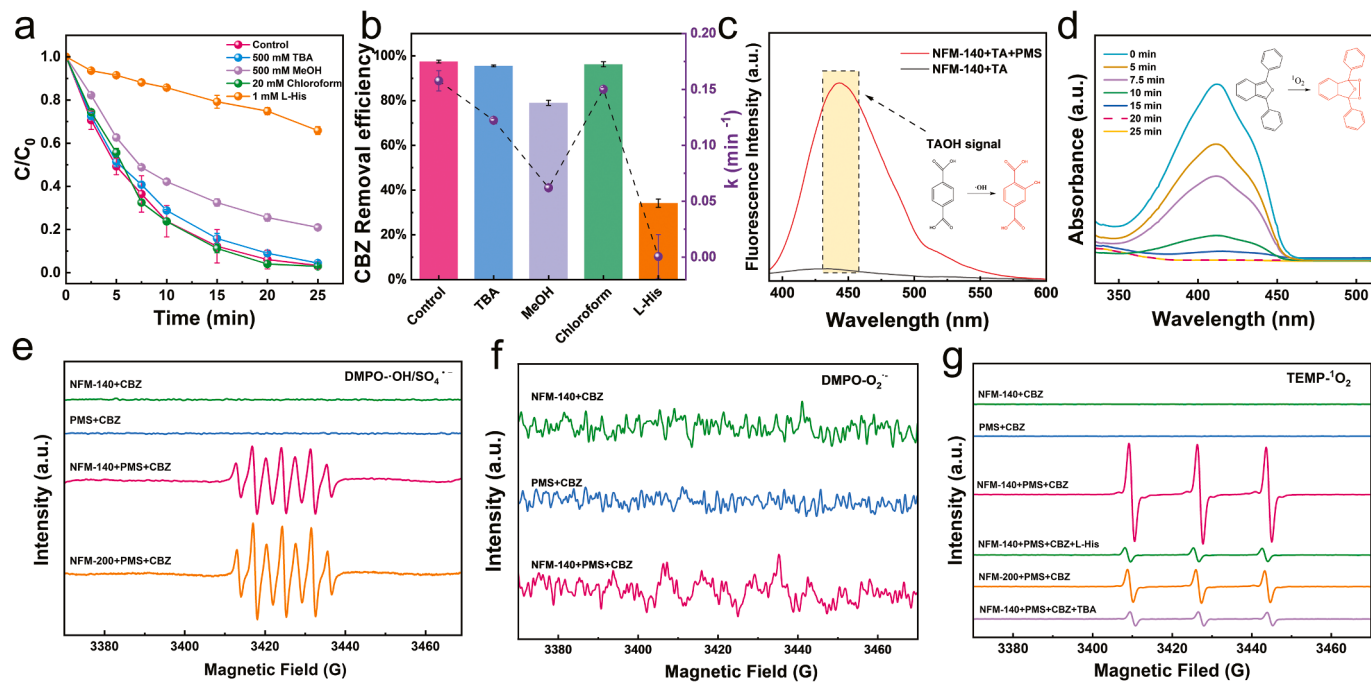


Fig. 3. a) Effects of scavengers (TBA, MeOH, chloroform, L-His) on the degradation of CBZ and b) the corresponding efficiency and k values of CBZ removal. c) Fluorescence spectra of terephthalic acid oxidized by NFM-140 in the presence of PMS (excitation wavelength: 319 nm). d) Absorption spectra recording the reaction of DPBF with $^1\text{O}_2$ generated upon NFM-140/PMS. EPR spectra for e) DMPO- SO_4^{2-} and DMPO- $\bullet\text{OH}$, f) DMPO- O_2^{2-} , g) TEMP- $^1\text{O}_2$.

the addition of CBZ, suggesting that $\text{MnO}_2-(\text{O})\text{OSO}_4^-$ is unable to extract electrons from CBZ for the direct electron transfer pathway (ETP). Open circuit potential (OCP) tests further confirm the formation of a high redox potential complex (0.9159 V) on the surface of NFM-140 after the introduction of PMS (Fig. S16a), and the unchanged OCP after the addition of CBZ is consistent with the in situ Raman results. Tan et al. [44] reported that the prerequisite of ETP is that the open circuit potential of the complex should exceed the oxidation potentials of organics. Therefore, based on chronoamperometry analysis (Text S5) and the high oxidation potential of CBZ (1.167 V > 0.9159 V) obtained by LSV (Fig. S16b), ETP is unlikely to occur in the NFM-140/PMS/CBZ system. To further investigate the ETP, a two-compartment current oxidation reactor was constructed by placing NFM-140 coated on carbon cloth electrodes into two cells of PMS and CBZ to form a closed circuit (Fig. S17a, Text S8), which ensures that CBZ can only be decomposed by ETP. However, the result obtained in Fig. S17b demonstrates that CBZ elimination depends completely on PMS-generated ROS ($^1\text{O}_2$) rather than the ETP process.

As a multivalent transition metal oxide, MnO_2 demonstrates its transition valence state in the activation of PMS. $\text{Mn}_{(s)}^{2+}$ can be originated from $\text{Mn}_{(s)}^{4+} \rightarrow \text{Mn}_{(s)}^{3+} \rightarrow \text{Mn}_{(s)}^{2+} \rightarrow \text{Mn}_{(aq)}^{2+}$ [45], but the Mn leaching (0.036 mg/L) and the formation of $\text{Mn}_{(aq)}^{2+}$ from $\text{Mn}_{(s)}^{2+}$ is negligible. $\text{Mn}_{(aq)}^{2+}$ shows marginal activity (Fig. S18a) and the irregular fitting results (Fig. S19a) means the Mn^{2+} delivers no contribution to the PMS activation. The reactivity of NFM catalysts shows a strong correlation with Mn^{3+} ($R^2=0.958$, Fig. S19b). Sodium pyrophosphate (PP) was used as a complexing agent for Mn^{3+} to verify the role of Mn^{3+} in the reaction [46]. The removal efficiency of CBZ (Fig. S18a-b) combined with the characteristic peak of the Mn^{3+} -PP complex at 258 nm (Fig. S20) confirm the crucialness of Mn^{3+} . Comparatively, Mn^{4+} as the transition state of Mn^{3+} , has low activity in the catalytic PMS reaction [47]. In addition, the high-valence Mn species on the surface of the NFM catalyst was captured using methyl phenyl sulfoxide (PMSO) [46], which can be oxidized to methyl phenyl sulfone (PMSO₂) through a reaction with Mn^{5+} [48]. Fig. S18c demonstrates that PMSO can be converted into PMSO₂ effectively by PMS. To be specific, the concentration of PMSO₂

produced provides conclusive evidence for the absence of high valent manganese species in the NFM/PMS system. Based on the above results, we can verify that Mn^{3+} is the pivotal valence state for PMS activation.

3.4. Effect of OV on $^1\text{O}_2$ formation

DFT calculations were applied to further reveal the effect of OV on the activation of PMS and the pathway of the generation of $^1\text{O}_2$ (see Text S6 for details). Based on the TEM results, a model labelled MnO_2 -OVs with OV was constructed on the (200) surface (represent the exposed (400) plane of NFM-140). The one without OV was named MnO_2 -P (Fig. S21). Compared to MnO_2 -P, MnO_2 -OVs has a lower adsorption energy (-1.50 eV vs. -1.48 eV) and a longer O-O bond length (1.4700 Å vs. 1.4663 Å), which can facilitate more efficient interaction and potentially contribute to enhanced activation of PMS (Fig. 4a-b) [33].

Furthermore, we propose the possible generation pathway of $^1\text{O}_2$ based the DFT calculations as follow: PMS \rightarrow *PMS \rightarrow *OH + $\text{SO}_4^{2-} \rightarrow$ *OH + $\text{H}_2\text{SO}_4 \rightarrow$ *O \rightarrow *OOH \rightarrow * $\text{O}_2 \rightarrow$ $^1\text{O}_2$ (Fig. 4c, Fig. S22). Firstly, PMS tends to bind to the site of the Mn atoms and spontaneously forms *OH and SO_4^{2-} to support the production of oxygenated intermediates (Step I). SO_4^{2-} is used to form H_2SO_4 via an exothermic reaction (Step II). The *OH is transferred to the other Mn atom or OV on MnO_2 to form *O after removal of the H from *OH (Step III). The *O reacts with PMS to form *OOH (Step IV). Subsequently, the *OOH reacts further to form * O_2 (Step V) and finally transforms into $^1\text{O}_2$ (Step VI). As summarized in Fig. 4d, the Gibbs free energies of all intermediates for the rest of the MnO_2 -P and MnO_2 -OVs reaction pathways were compared. The *OH \rightarrow *O step is the rate limiting step with the highest energy barrier during the multistep $^1\text{O}_2$ formation process. The presence of OV can reduce the free energy barriers (2.19 eV vs. 2.37 eV) in this step, thereby facilitating the formation of $^1\text{O}_2$ in the subsequent steps. The above theoretical results show that the introduction of OV into the MnO_2 is conducive to enhancing the adsorption and decomposition of PMS molecules. This process thermodynamically generates the intermediate *O and facilitates the rapid formation of $^1\text{O}_2$. Therefore, radicals are

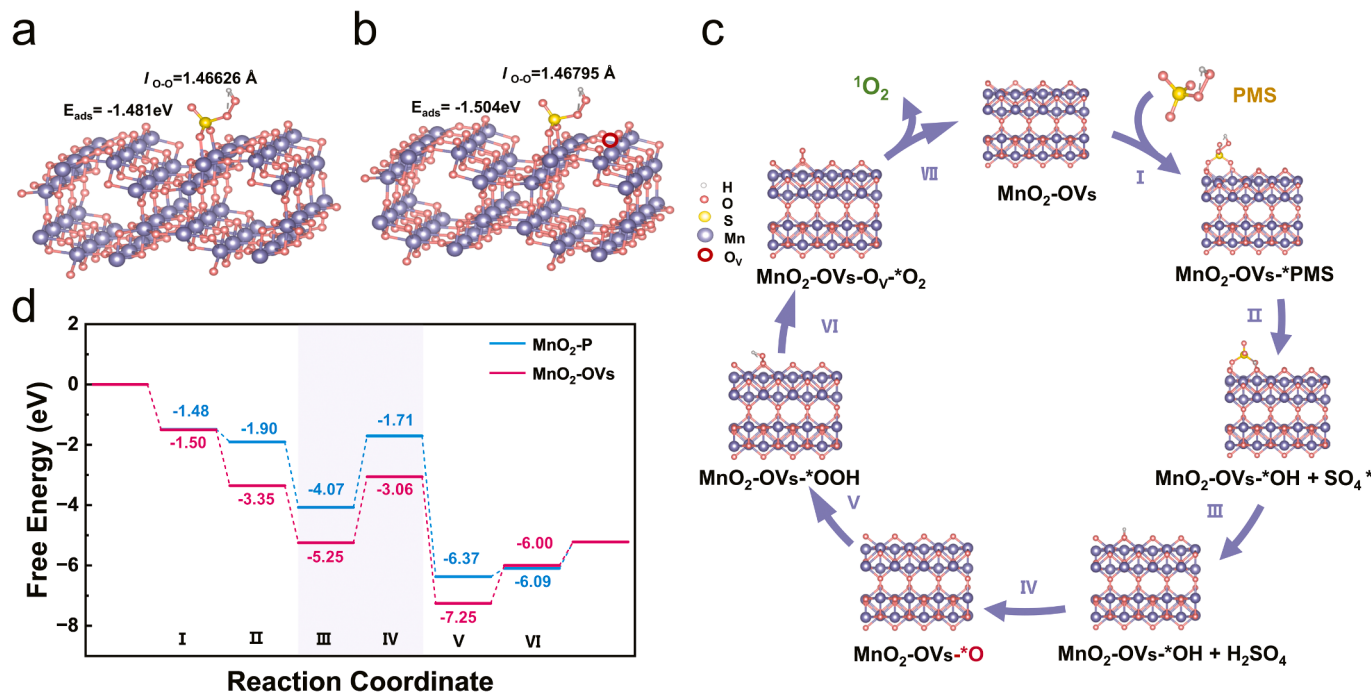
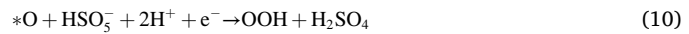
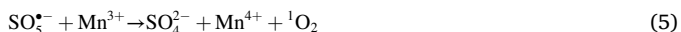


Fig. 4. The sketch map of the adsorption of PMS on (400) plane in α -MnO₂ a) without or b) with OVs. c) Proposed reaction process for SO₄^{*} and *OH moieties oxidation to 1O_2 on MnO₂-OVs. d) The calculated Gibbs free energy diagrams for the rate-determining step based on SO₄^{*} and *OH moieties oxidation to 1O_2 on MnO₂-P and MnO₂-OVs.

more inclined to further generate 1O_2 on the materials with more OVs, while they are more likely to react with pollutants rather than subsequent transformations on the materials with less OVs.

According to the above experiment results, the possible mechanisms of CBZ degradation by the NFM/PMS system are proposed. Mn³⁺ and OVs on the surface of as-prepared NFM catalysts are the dominant active site for PMS activation. Specifically, the redox electrons are transferred to PMS through oxidation of Mn³⁺ to Mn⁴⁺. HSO₅⁻ is activated to produce SO₄²⁻ and \bullet OH radicals (Eqs. 1 and 2), part of Mn⁴⁺ and Mn³⁺ is converted to Mn³⁺ and Mn²⁺ in the presence of HSO₅⁻ (Eqs. 3 and 4) [49]. And 1O_2 can be produced by the reaction between Mn³⁺ and SO₅²⁻ (Eq. 5) [28]. OVs promotes the adsorption of PMS on the catalyst surface to decompose and produce 1O_2 directly (Eq. 6) [50]. *O from O_L and *OH will be turned into 1O_2 through the OVs easily with lower Gibbs free energy (Eqs. 7–12) [31,51], resulting in the consumption of OVs (Fig. S23). In the NFM/PMS/CBZ degradation system, the high redox potential of CBZ prevents ETP from directly removal of CBZ, so ROS is the driving force supporting the elimination process. Compared with low concentration free radicals, the non-radical pathway dominated by 1O_2 is the main ROS CBZ degradation.



3.5. Degradation pathway of CBZ

The possible degradation pathways of the CBZ molecule (Fig. 5a) were elucidated using the DFT Fukui method. We calculated the frontier electron densities of the highest occupied molecular orbital (HOMO, Fig. 5b) and the lowest unoccupied molecular orbital (LUMO, Fig. 5c) to analyze the easy and lost electrons or electron sites [52]. HOMO in Fig. 5b indicates that the electron-rich area located in center rings is vulnerable to the attack of electrophilic ROS. However, HOMO and LUMO fail to describe the active sites accurately. Thus, the natural population analysis (NPA) charge distribution and corresponding Fukui index were calculated for the further accurate investigation. The susceptibility of C(7) and C(8) atoms to free radical, electrophilic, and nucleophilic attacks is demonstrated by their higher f^0/f^- values (Fig. 5d) [53]. The Laplacian bond order (LBO) values can be used to assess the strength of each bond in the CBZ molecule. A lower LBO value typically signifies a weaker bond. As illustrated in Fig. 5e, the chemical bonds of (4) C-N (15), (10) C-N (15), (16) C-N (15) and (16) C-N (18) in the CBZ molecule can be easily broken due to their lower LBO values.

To further investigate the degradation process, LC-MS (Text S4) was performed to detect the intermediates of CBZ degradation (Fig. S24). We propose two pathways: pathway I (TP1 to TP6) and pathway II (TP7 to TP9) as shown in Fig. 5f. In degradation path I, ROS attacks the olefin double bond at sites (7) C and C (8) of CBZ to form TP1. The epoxy bond of TP1 is hydrolyzed to TP2 and then converted into a dialdehyde compound TP3 during ring opening. TP3 undergoes intramolecular cyclization via electrophilic aromatic substitution to form TP4. Subsequently, the acetyl and aldehyde groups are cleaved to form TP5 and

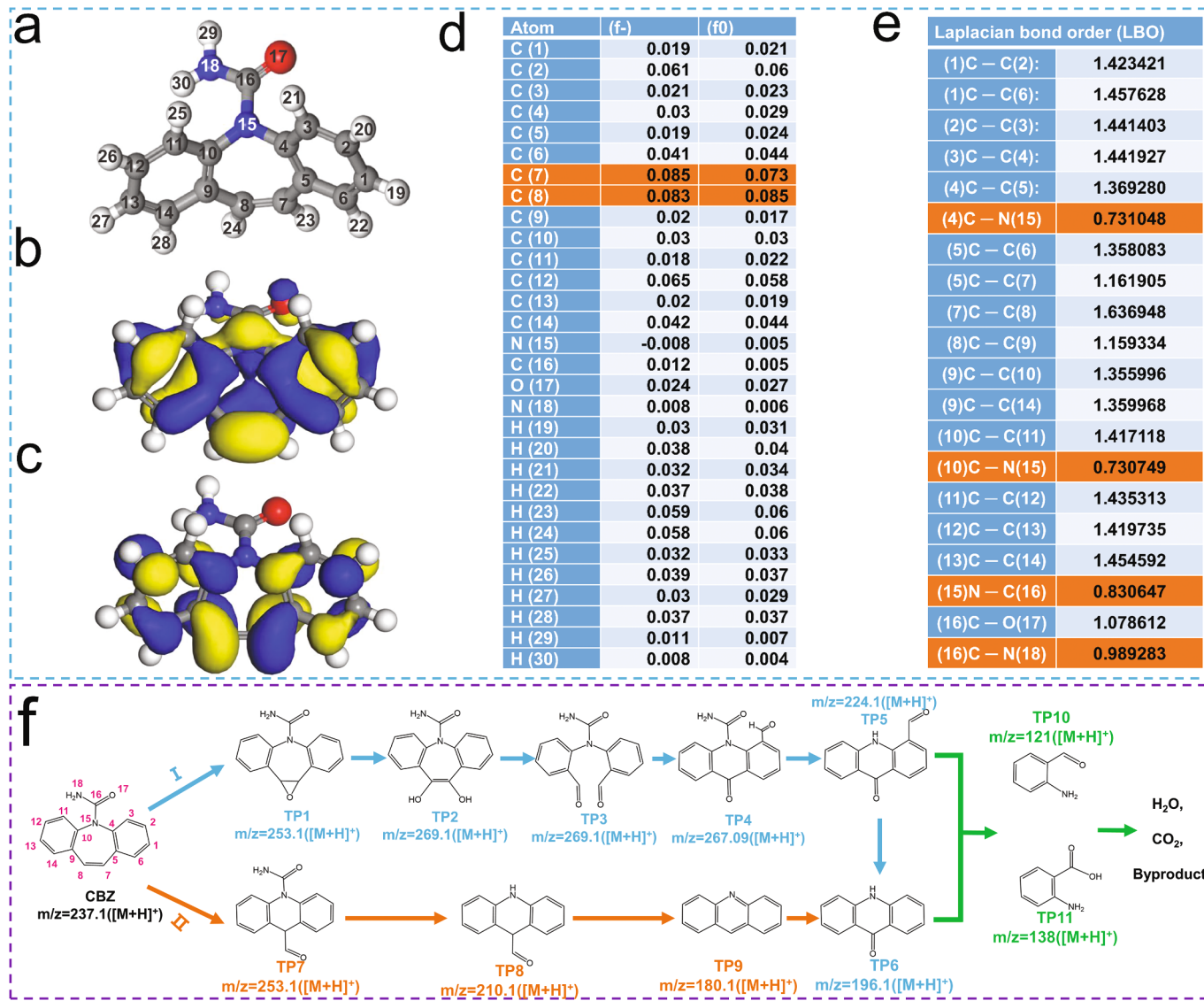


Fig. 5. a) CBZ chemical structure; b) HOMO, c) LUMO, d) Fukui index and e) LBO values of CBZ. f) Degradation pathway of CBZ.

TP6. In degradation pathway II, ROS attack cleaves the (16) C-N (18) bond of TP7 to form TP8. The aldehyde group of TP8 is then cleaved to form TP9, which is further oxidized to obtain TP6. Finally, ROS continue to attack these intermediates, producing the small molecules TP10 and TP11, which are eventually decomposed into CO₂, H₂O, and other byproducts. The degradation pathway involves the attack of ROS on (7) C, C (8), and (16) C-N (18), which is consistent with the DFT calculation results.

3.6. Environmental applications of NFM-140

Practical simulations were conducted to test the NFM-140/PMS system's effectiveness in the presence of natural organic matter (HA), anions (Cl⁻, SO₄²⁻, NO₃⁻), and different water matrices (tap water, Gan River water) (Figs. S25-26 and Table S5). The system demonstrates robust resistance to environmental disturbances and remained effective within a pH range of 3–9. In batch experiments, CBZ is efficiently removed with a mineralization rate of 64%, as detected by TOC analysis (Fig. S27). The NFM-140/PMS/CBZ system consumes 74% of the PMS concentration (Fig. S28). The excellent PMS decomposition efficiency reduces the cost of wastewater treatment and the generation of undesirable sulfate products, which is conducive to the purification of the

water environment.

The ecological structure activity relationships (ECOSAR) class program was applied to predict the toxicity of CBZ and its degradation products [54] (Fig. 6a, Table S6). Obviously, CBZ is a toxic chemical and most of the intermediates (TP1, TP2, TP3, TP4 and TP7) are less toxic than it, some toxic intermediates (TP5, TP9) will be subsequently converted to harmless products (TP10, TP11) in the NFM-140/PMS degradation system. *Escherichia coli* (*E. coli*) growth was used to test the biotoxicity of CBZ products at different reaction times (Text S9). *E. coli* growth in CBZ-25-minute reaction solution is almost close to the original density (Fig. 6b), there is no doubt that the NFM-140/PMS system significantly reduces the environmental hazard of CBZ.

NFM-140 maintains excellent performance (Fig. S29) and stable membrane morphology (Fig. S30) after eight cycles, and the concentration of Mn leaching is lower than 0.1 mg/L (Table S7). Moreover, the NFM-140 membrane reactor can achieve over 95% removal efficiency for a wide range of organic pollutants including TC, AO7, RhB, BPA, and Phenol (Fig. S31). 20 ppm RhB in Gan River water (Jiangxi, China) was used as simulate wastewater to further evaluate the environmental applications of NFM-140 (Text S10 for details). As shown in Video S1, the rapid discoloration of RhB by the NFM-140/PMS membrane reactor indicates its excellent potential in water treatment.

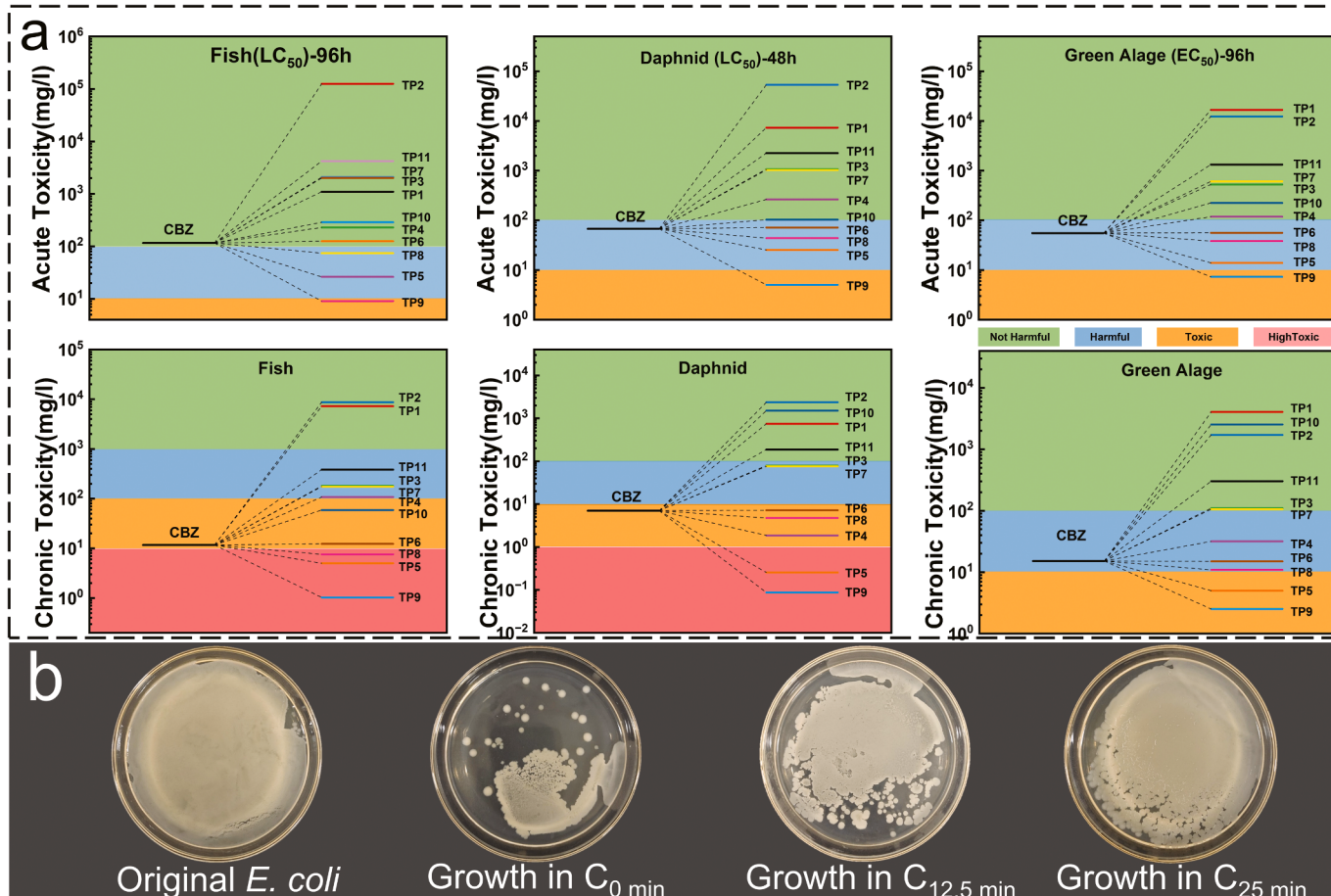


Fig. 6. Toxicity test: a) theoretically predicted results of acute/chronic toxicity of CBZ and its reaction products to Fish, Daphnid and Green Algae, b) Escherichia coli (*E. coli*) growth in corresponding degradation periods (0, 12.5 and 25 min) of CBZ solution. The toxicity includes four levels of harmless (>100 mg/L), harmful (10–100 mg/L), toxic (1–10 mg/L) and extremely toxic (<1 mg/L).

Supplementary material related to this article can be found online at doi:10.1016/j.apcatb.2024.124106.

4. Conclusion

In conclusion, the MnO₂ nanofiber membrane reactor with adjustable OVs concentration was designed in this study and exhibited high catalytic performance in activating PMS for effective CBZ removal through the ¹O₂ dominated non-radical pathways. The effective redox reactions between Mn³⁺ and Mn⁴⁺ contribute to the generation of ROS. OVs promote the adsorption of PMS on the catalyst surface and the release of O₂, the lower Gibbs free energy is conducive to the conversion of *OH to *O through OVs, thus facilitating the generation of ¹O₂. The membrane reactor is highly resistant to interference and shows great potential of practical applications due to its stability and capacity to remove a diverse array of pollutants. The result obtained in this research will contribute to the development of more active "defective" catalysts for the elimination of a variety of recalcitrant organics for sustainable wastewater treatment.

CRediT authorship contribution statement

Yichuan Wang: Writing – original draft, Methodology, Investigation, Data curation, Conceptualization. **Tianlin Zhou:** Writing – original draft, Validation, Methodology, Investigation, Data curation. **Dezhi Chen:** Writing – review & editing, Supervision, Project administration, Investigation, Funding acquisition, Conceptualization. **Zhi-Xia Zhang:** Validation, Supervision, Resources, Investigation. **Quanzhi Zhang:**

Software, Investigation, Data curation. **Xinchun Ye:** Software, Investigation, Data curation. **Jianjun Wan:** Validation, Investigation, Data curation. **Jian-Ping Zou:** Writing – review & editing, Supervision, Project administration, Conceptualization.

Declaration of Competing Interest

The authors declare that they have no known competing financial interests or personal relationships that could have appeared to influence the work reported in this paper.

Data availability

Data will be made available on request.

Acknowledgements

This work was supported by the Major Discipline Academic and Technical Leaders Training Program (20232BCJ22015) of Jiangxi Province, China, and National Natural Science Foundation (51968049) of China.

Appendix A. Supporting information

Supplementary data associated with this article can be found in the online version at doi:10.1016/j.apcatb.2024.124106.

References

- [1] M. Li, Z. Li, X. Yu, Y. Wu, C. Mo, M. Luo, L. Li, S. Zhou, Q. Liu, N. Wang, K. Lun Yeung, S. Chen, FeN₄-doped carbon nanotubes derived from metal organic frameworks for effective degradation of organic dyes by peroxymonosulfate: Impacts of FeN₄ spin states, *Chem. Eng. J.* 431 (2022) 133339, <https://doi.org/10.1016/j.cej.2021.133339>.
- [2] M.S. Lucas, J.A. Peres, G. Li Puma, Advanced oxidation processes for water and wastewater treatment, *Water* 13 (2021) 1309, <https://doi.org/10.3390/w13091309>.
- [3] S. Xiao, M. Cheng, H. Zhong, Z.F. Liu, Y. Liu, X. Yang, Q.H. Liang, Iron-mediated activation of persulfate and peroxymonosulfate in both homogeneous and heterogeneous ways: a review, *Chem. Eng. J.* 384 (2020) 123265, <https://doi.org/10.1016/j.cej.2019.123265>.
- [4] J. Ding, J. Wang, X. Luo, D. Xu, Y. Liu, P. Li, S. Li, R. Wu, X. Gao, H. Liang, A passive-active combined strategy for ultrafiltration membrane fouling control in continuous oily wastewater purification, *Water Res.* 226 (2022) 119219, <https://doi.org/10.1016/j.watres.2022.119219>.
- [5] Y. Liu, Q. Lin, Y. Guo, J. Zhao, X. Luo, H. Zhang, G. Li, H. Liang, The nitrogen-doped multi-walled carbon nanotubes modified membrane activated peroxymonosulfate for enhanced degradation of organics and membrane fouling mitigation in natural waters treatment, *Water Res.* 209 (2022) 117960, <https://doi.org/10.1016/j.watres.2021.117960>.
- [6] S.P. Mo, Q. Zhang, J.Q. Li, Y.H. Sun, Q.M. Ren, S.B. Zou, Q. Zhang, J.H. Lu, M. L. Fu, D.Q. Mo, J.L. Wu, H.M. Huang, D.Q. Ye, Highly efficient mesoporous MnO₂ catalysts for the total toluene oxidation: oxygen-vacancy defect engineering and involved intermediates using *in situ* DRIFTS, *Appl. Catal. B* 264 (2020) 118464, <https://doi.org/10.1016/j.apcatb.2019.118464>.
- [7] T. Zhang, Y. Chen, T. Leiknes, Oxidation of refractory benzothiazoles with PMS/CuFe₂O₄: Kinetics and transformation intermediates, *Environ. Sci. Technol.* 50 (2016) 5864–5873, <https://doi.org/10.1021/acs.est.6b00701>.
- [8] A.R. Lado Ribeiro, N.F.F. Moreira, G. Li Puma, A.M.T. Silva, Impact of water matrix on the removal of micropollutants by advanced oxidation technologies, *Chem. Eng. J.* 363 (2019) 155–173, <https://doi.org/10.1016/j.cej.2019.01.080>.
- [9] Z.C. Yang, J.S. Qian, C. Shan, H.C. Li, Y.Y. Yin, B.C. Pan, Toward selective oxidation of contaminants in aqueous systems, *Environ. Sci. Technol.* 55 (2021) 14494–14514, <https://doi.org/10.1021/acs.est.1c05862>.
- [10] X.G. Duan, H.Q. Sun, Z.P. Shao, S.B. Wang, Nonradical reactions in environmental remediation processes: Uncertainty and challenges, *Appl. Catal. B* 224 (2018) 973–982, <https://doi.org/10.1016/j.apcatb.2017.11.051>.
- [11] B. Wang, Y.M. Lee, W.Y. Tcho, S. Tussupbayev, S.T. Kim, Y. Kim, M.S. Seo, K. B. Cho, Y. Dede, B.C. Keegan, T. Ogura, S.H. Kim, T. Ohta, M.H. Baik, K. Ray, J. Shearer, W. Nam, Synthesis and reactivity of a mononuclear non- haem cobalt (IV)-oxo complex, *Nat. Commun.* 8 (2017), <https://doi.org/10.1038/ncomms14839>.
- [12] J. Pei, K. Fu, Y. Fu, X. Liu, S. Luo, K. Yin, J. Luo, Manipulating high-valent cobalt-oxo generation on Co/N codoped carbon beads via PMS activation for micropollutants degradation, *ACS Est. Eng.* 3 (2023) 1997–2007, <https://doi.org/10.1021/acs.estengg.3c00295>.
- [13] R. Li, Y. Huang, D.D. Zhu, W.K. Ho, J.J. Cao, S.C. Lee, Improved oxygen activation over a carbon/Co₃O₄ nanocomposite for efficient catalytic oxidation of formaldehyde at room temperature, *Environ. Sci. Technol.* 55 (2021) 4054–4063, <https://doi.org/10.1021/acs.est.1c00490>.
- [14] L.Y. Wu, J.M. Hong, Q. Zhang, B.Y. Chen, J. Wang, Z.Y. Dong, Deciphering highly resistant characteristics to different pHs of oxygen vacancy-rich Fe₂Co₁-LDH/PS system for bisphenol A degradation, *Chem. Eng. J.* 385 (2020) 123620, <https://doi.org/10.1016/j.cej.2019.123620>.
- [15] J.L. Sheng, A.M. Lu, S.K. Guo, Y. Shi, H. Wu, H.M. Jiang, Superior benzulfuron-methyl degradation performance of spherical magnetic Co₃O₄@C-500/ peroxymonosulfate system by enhancing singlet oxygen generation: The effect of oxygen vacancies, *Chem. Eng. J.* 471 (2023) 143945, <https://doi.org/10.1016/j.cej.2023.143945>.
- [16] T.O. Owolabi, T.F. Qahtan, O.R. Abidemi, T.A. Saleh, O.W. Adeyemi, Bismuth oxychloride photocatalytic wide band gap adjustment through oxygen vacancy regulation using a hybrid intelligent computational method, *Mater. Chem. Phys.* 290 (2022) 126524, <https://doi.org/10.1016/j.matchemphys.2022.126524>.
- [17] L.L. Liang, P.K. Cao, X. Qin, S. Wu, H.K. Bai, S. Chen, H.T. Yu, Y. Su, X. Quan, Oxygen vacancies-driven nonradical oxidation pathway of catalytic ozonation for efficient water decontamination, *Appl. Catal. B* 325 (2023) 122321, <https://doi.org/10.1016/j.apcatb.2022.122321>.
- [18] J.J. Wang, X.L. Xu, Y.Y. Liu, Z.Y. Wang, P. Wang, Z.K. Zheng, H.F. Cheng, Y. Dai, B. B. Huang, Oxygen-vacancy-enhanced singlet oxygen production for selective photocatalytic oxidation, *Chemsuschem* 13 (2020) 3488–3494, <https://doi.org/10.1002/cssc.202000595>.
- [19] Y.G. Bu, H.C. Li, W.J. Yu, Y.F. Pan, L.J. Li, Y.F. Wang, L.T. Pu, J. Ding, G.D. Gao, B. C. Pan, Peroxydisulfate activation and singlet oxygen generation by oxygen vacancy for degradation of contaminants, *Environ. Sci. Technol.* 55 (2021) 2110–2120, <https://doi.org/10.1021/acs.est.0c07274>.
- [20] P.E. Blöchl, Projector augmented-wave method, *Phys. Rev. B* 50 (1994) 17953–17979, <https://doi.org/10.1103/PhysRevB.50.17953>.
- [21] D.J. Chadi, Special points for Brillouin-zone integrations, *Phys. Rev. B* 16 (1977) 1746–1747, <https://doi.org/10.1103/PhysRevB.16.1746>.
- [22] E. Skúlason, G.S. Karlberg, J. Rossmeisl, T. Bligaard, J. Greeley, H. Jónsson, J. K. Norskov, Density functional theory calculations for the hydrogen evolution reaction in an electrochemical double layer on the Pt(111) electrode, *Phys. Chem. Chem. Phys.* 9 (2007) 3241–3250, <https://doi.org/10.1039/b700099e>.
- [23] J. Ye, C.X. Li, L.L. Wang, Y.S. Yan, Y. Wang, J.D. Dai, MOFs derived 3D sea urchin-like carbon frameworks loaded on PVDF membranes as PMS activator for highly efficient bisphenol A degradation, *Sep. Purif. Technol.* 258 (2021) 117669, <https://doi.org/10.1016/j.seppur.2020.117669>.
- [24] Y. Kumar, S. Chopra, A. Gupta, Y. Kumar, S.J. Uke, S.P. Mardikar, Low temperature synthesis of MnO₂ nanostructures for supercapacitor application, *Mater. Sci. Energy Technol.* 3 (2020) 566–574, <https://doi.org/10.1016/j.mset.2020.06.002>.
- [25] W. Kong, L. Huang, X. Quan, G.L. Puma, Synergistic induced charge transfer switch by oxygen vacancy and pyrrolic nitrogen in MnFe₂O₄/g-C₃N₄ heterojunctions for efficient transformation of bicarbonate to acetate in photo-assisted MES, *Appl. Catal. B* 307 (2022) 121214, <https://doi.org/10.1016/j.apcatb.2022.121214>.
- [26] C. Dong, H. Wang, Y.W. Ren, Z.P. Qu, Layer MnO₂ with oxygen vacancy for improved toluene oxidation activity, *Surf. Interface Anal.* 22 (2021) 100897, <https://doi.org/10.1016/j.surfin.2020.100897>.
- [27] J.B. Jia, P.Y. Zhang, L. Chen, Catalytic decomposition of gaseous ozone over manganese dioxides with different crystal structures, *Appl. Catal. B* 189 (2016) 210–218, <https://doi.org/10.1016/j.apcatb.2016.02.055>.
- [28] H. Yi, Y. Wang, L. Diao, Y. Xin, C. Chai, D. Cui, D. Ma, Ultrasonic treatment enhances the formation of oxygen vacancies and trivalent manganese on alpha-Mn₂O₃ surfaces: Mechanism and application, *J. Colloid Interface Sci.* 626 (2022) 629–638, <https://doi.org/10.1016/j.jcis.2022.06.144>.
- [29] M. Zhao, R. Xu, Z. Chen, Z. Gao, S. Zheng, H. Song, Kinetics and mechanisms of diniconazole degradation by α -MnO₂ activated peroxymonosulfate, *Sep. Purif. Technol.* 281 (2022) 119850, <https://doi.org/10.1016/j.seppur.2021.119850>.
- [30] C. Dong, H. Wang, Y. Ren, Z. Qu, Effect of alkaline earth metal promoter on catalytic activity of MnO₂ for the complete oxidation of toluene, *J. Environ. Sci.* 104 (2021) 102–112, <https://doi.org/10.1016/j.jes.2020.11.003>.
- [31] Y. Wang, M. Liu, C. Hu, Y. Xin, D. Ma, M. Gao, H. Xie, Enhanced MnO₂/ peroxymonosulfate activation for phthalic acid esters degradation: Regulation of oxygen vacancy, *Chem. Eng. J.* 433 (2022) 134048, <https://doi.org/10.1016/j.cej.2021.134048>.
- [32] S. Shen, X. Zhou, Q. Zhao, W. Jiang, J. Wang, L. He, Y. Ma, L. Yang, Z. Chen, Understanding the nonradical activation of peroxymonosulfate by different crystallographic MnO₂: The pivotal role of Mn(III) content on the surface, *J. Hazard. Mater.* 439 (2022) 129613, <https://doi.org/10.1016/j.jhazmat.2022.129613>.
- [33] M. Li, S. You, X. Duan, Y. Liu, Selective formation of reactive oxygen species in peroxymonosulfate activation by metal-organic framework-derived membranes: A defect engineering-dependent study, *Appl. Catal. B* 312 (2022) 121419, <https://doi.org/10.1016/j.apcatb.2022.121419>.
- [34] Y. Liu, J. Luo, L. Tang, C. Feng, J. Wang, Y. Deng, H. Liu, J. Yu, H. Feng, J. Wang, Origin of the enhanced reusability and electron transfer of the carbon-coated Mn₃O₄ nanocube for persulfate activation, *ACS Catal.* 10 (2020) 14857–14870, <https://doi.org/10.1021/acscatal.0c04049>.
- [35] W. Huang, M. Brigante, F. Wu, C. Mousty, K. Hanna, G. Mailhot, Assessment of the Fe(III)-EDDS complex in Fenton-like processes: from the radical formation to the degradation of bisphenol A, *Environ. Sci. Technol.* 47 (2013) 1952–1959, <https://doi.org/10.1021/es304502y>.
- [36] S. Lu, G. Wang, S. Chen, H. Yu, F. Ye, X. Quan, Heterogeneous activation of peroxymonosulfate by LaCo_{1-x}Cu_xO₃ perovskites for degradation of organic pollutants, *J. Hazard. Mater.* 353 (2018) 401–409, <https://doi.org/10.1016/j.jhazmat.2018.04.021>.
- [37] X. Wang, Y. Qin, L. Zhu, H. Tang, Nitrogen-doped reduced graphene oxide as a bifunctional material for removing bisphenols: Synergistic effect between adsorption and catalysis, *Environ. Sci. Technol.* 49 (2015) 6855–6864, <https://doi.org/10.1021/acs.est.5b01059>.
- [38] H. Zhou, L. Xiao, Y. Deng, C. Chen, X. Pei, Q. Li, Y. Ye, F. Pan, Revisiting the multipath elimination of contaminants by carbonyl-containing manganese-carbon composites in the peroxymonosulfate system: A new way of constructing C-Mn-PMS complexes to distinguish the stages of active species production, *Chem. Eng. J.* 471 (2023) 144685, <https://doi.org/10.1016/j.cej.2023.144685>.
- [39] Y. Gao, T. Wu, C. Yang, C. Ma, Z. Zhao, Z. Wu, S. Cao, W. Geng, Y. Wang, Y. Yao, Y. Zhang, C. Cheng, Activity trends and mechanisms in peroxymonosulfate-assisted catalytic production of singlet oxygen over atomic metal-N-C catalysts, *Angew. Chem. Int. Ed.* 60 (2021) 22513–22521, <https://doi.org/10.1002/anie.202109530>.
- [40] S. Zhang, Y. Liu, P. Gu, R. Ma, T. Wen, G. Zhao, L. Li, Y. Ai, C. Hu, X. Wang, Enhanced photodegradation of toxic organic pollutants using dual-oxygen-doped porous g-C₃N₄: Mechanism exploration from both experimental and DFT studies, *Appl. Catal. B* 248 (2019) 1–10, <https://doi.org/10.1016/j.apcatb.2019.02.008>.
- [41] Z. Wang, Y. Lin, S. Guo, X. Zhang, Q. Guo, Y. Luo, X. Ou, J. Ma, Y. Zhou, J. Jiang, B. Han, Site engineering of covalent organic frameworks for regulating peroxymonosulfate activation to generate singlet oxygen with 100 % selectivity, *Angew. Chem. Int. Ed.* 62 (2023) e202310934, <https://doi.org/10.1002/anie.202310934>.
- [42] Y. Wang, M. Liu, C. Hu, Y. Xin, D. Ma, M. Gao, H. Xie, Enhanced MnO₂/ peroxymonosulfate activation for phthalic acid esters degradation: Regulation of oxygen vacancy, *Chem. Eng. J.* 433 (2022) 134048, <https://doi.org/10.1016/j.cej.2021.134048>.
- [43] J. Dou, Y. Tang, Z. Lu, G. He, J. Xu, Y. He, Neglected but efficient electron utilization driven by biochar-coactivated phenols and peroxydisulfate: Polyphenol accumulation rather than mineralization, *Environ. Sci. Technol.* 57 (2023) 5703–5713, <https://doi.org/10.1021/acs.est.3c00022>.
- [44] W. Tan, W. Ren, C. Wang, Y. Fan, B. Deng, H. Lin, H. Zhang, Peroxymonosulfate activated with waste battery-based Mn-Fe oxides for pollutant removal: Electron transfer mechanism, selective oxidation and LFER analysis, *Chem. Eng. J.* 394 (2020) 124864, <https://doi.org/10.1016/j.cej.2020.124864>.

[45] Y. Yang, P. Zhang, K. Hu, X. Duan, Y. Ren, H. Sun, S. Wang, Sustainable redox processes induced by peroxymonosulfate and metal doping on amorphous manganese dioxide for nonradical degradation of water contaminants, *Appl. Catal. B* 286 (2021), <https://doi.org/10.1016/j.apcatb.2021.119903>.

[46] Y. Zhu, H. Ding, J. Fan, S. Liu, Y. Song, H. Deng, C. Zhao, D.D. Dionysiou, Nonradical activation of peroxydisulfate with in situ generated amorphous MnO_2 in an electro-permanganate process: involvement of singlet oxygen, electron transfer, and $Mn(III)aq$, *ACS Est. Eng.* 2 (2022) 1316–1325, <https://doi.org/10.1021/acsestengg.1c00464>.

[47] H. Ouyang, C. Wu, X.H. Qiu, K. Tanaka, T. Ohnuki, Q.Q. Yu, New insight of $Mn(III)$ in delta- MnO_2 for peroxymonosulfate activation reaction: Via direct electron transfer or via free radical reactions, *Environ. Res.* 217 (2023) 114874, <https://doi.org/10.1016/j.envres.2022.114874>.

[48] P. Zhou, Y. Yang, W. Ren, X. Li, Y. Zhang, B. Lai, S. Wang, X. Duan, Molecular and kinetic insights to boron boosted Fenton-like activation of peroxymonosulfate for water decontamination, *Appl. Catal. B* 319 (2022) 121916, <https://doi.org/10.1016/j.apcatb.2022.121916>.

[49] Y. Chi, P. Wang, M. Lin, C. Lin, M. Gao, C. Zhao, X. Wu, Manganese oxides activated peroxymonosulfate for ciprofloxacin removal: Effect of oxygen vacancies and chemical states, *Chemosphere* 299 (2022) 134437, <https://doi.org/10.1016/j.chemosphere.2022.134437>.

[50] Y. Wang, Y. Sun, R. Wang, M. Gao, Y. Xin, G. Zhang, P. Xu, D. Ma, Activation of peroxymonosulfate with cobalt embedded in layered $\delta-MnO_2$ for degradation of dimethyl phthalate: Mechanisms, degradation pathway, and DFT calculation, *J. Hazard. Mater.* 451 (2023) 130901, <https://doi.org/10.1016/j.jhazmat.2023.130901>.

[51] G. Chen, Y. Sun, R.R. Chen, C. Biz, A.C. Fisher, M.P. Sherburne, J.W. Ager Iii, J. Gracia, Z.J. Xu, A discussion on the possible involvement of singlet oxygen in oxygen electrocatalysis, *J. Phys. -Energy* 3 (2021) 031004, <https://doi.org/10.1088/2515-7655/abe039>.

[52] C. Pan, Y. Sun, Y. Dong, H. Hou, M.F. Kai, J. Lan, Efficient carbamazepine degradation by modified copper tailings and PMS system: Performance evaluation and mechanism, *J. Hazard. Mater.* 465 (2024) 133198, <https://doi.org/10.1016/j.jhazmat.2023.133198>.

[53] A.D. Isravel, J.K. Jeyaraj, S. Thangasamy, W.J. John, DFT, NBO, HOMO-LUMO, NCI, stability, Fukui function and hole-electron analyses of tolcapone, *Comput. Theor.* 1202 (2021) 113296, <https://doi.org/10.1016/j.comptc.2021.113296>.

[54] X. Luo, Y. You, M. Zhong, L. Zhao, Y. Liu, R. Qiu, Z. Huang, Green synthesis of manganese-cobalt-tungsten composite oxides for degradation of doxycycline via efficient activation of peroxymonosulfate, *J. Hazard. Mater.* 426 (2022) 127803, <https://doi.org/10.1016/j.jhazmat.2021.127803>.